Astronomy
&
Astrophysics

The massive binary CPD – 41° 7742

II. Optical light curve and X-ray observations[*]

H. Sana[1,**], E. Antokhina[2], P. Royer[3], J. Manfroid[1,***], E. Gosset[1,†], G. Rauw[1,†], and J.-M. Vreux[1]

[1] Institut d'Astrophysique et de Géophysique, Université de Liège, Allée du 6 Août 17, Bât. B5c, 4000 Liège, Belgium
    e-mail: [sana;manfroid;gosset;rauw;vreux]@astro.ulg.ac.be
[2] Sternberg Astronomical Institute, Moscow State University, Universitetskii Pr., 13, 119899 Moscow, Russia
    e-mail: elant@sai.msu.ru
[3] Instituut voor Sterrenkunde, Katholieke Universiteit Leuven, Celestijnenlaan 200 B, 3001 Leuven, Belgium
    e-mail: pierre@ster.kuleuven.ac.be

Abstract. In the first paper of this series, we presented a detailed high-resolution spectroscopic study of CPD – 41° 7742, deriving for the first time an orbital solution for both components of the system. In this second paper, we focus on the analysis of the optical light curve and on recent XMM-*Newton* X-ray observations. In the optical, the system presents two eclipses, yielding an inclination $i \sim 77°$. Combining the constraints from the photometry with the results of our previous work, we derive the absolute parameters of the system. We confirm that the two components of CPD – 41° 7742 are main sequence stars (O9 V + B1–1.5 V) with masses ($M_1 \sim 18\ M_\odot$ and $M_2 \sim 10\ M_\odot$) and respective radii ($R_1 \sim 7.5\ R_\odot$ and $R_2 \sim 5.4\ R_\odot$) close to the typical values expected for such stars.

We also report an unprecedented set of X-ray observations that almost uniformly cover the 2.44-day orbital cycle. The X-ray emission from CPD – 41° 7742 is well described by a two-temperature thermal plasma model with energies close to 0.6 and 1.0 keV, thus slightly harder than typical early-type emission. The X-ray light curve shows clear signs of variability. The emission level is higher when the primary is in front of the secondary. During the high emission state, the system shows a drop of its X-ray emission that almost exactly matches the optical eclipse. We interpret the main features of the X-ray light curve as the signature of a wind-photosphere interaction, in which the overwhelming primary O9 star wind crashes into the secondary surface. Alternatively the light curve could result from a wind-wind interaction zone located near the secondary star surface. As a support to our interpretation, we provide a phenomenological geometric model that qualitatively reproduces the observed modulations of the X-ray emission.

Key words. stars: individual: CPD – 41° 7742 – stars: binaries: close – stars: binaries: eclipsing – stars: early-type – stars: fundamental parameters – X-rays: stars

1. Introduction

In the quest for accurate measurements of fundamental stellar parameters, eclipsing spectroscopic binaries are unique physical laboratories all over the Hertzsprung-Russell diagram. Combined spectroscopic and photometric studies provide a direct determination of the masses and sizes of their stellar components. This is of a particular interest in the upper left part of the diagram. Although few in number, massive early-type stars have a large influence on their surroundings through their mechanical and radiative energy input. A detailed knowledge of both their evolution and wind properties is thus crucial in many different contexts. For example, these objects seem to play a key role in the formation of the less massive stars in starburst regions or within the core of OB associations. However, our understanding of massive stars is clearly still fragmentary. Only a few tens of objects have their orbital and physical parameters determined with a reasonable accuracy (Gies 2003). The problem of their exact formation mechanism is largely unsolved (Zinnecker 2003) and, from the theoretical point of view, their physical parameters (effective temperatures, radii, masses, ...) significantly differ from one study to another (Humphreys & McElroy 1984; Howarth & Prinja 1989; Vacca et al. 1996). The observational masses deduced from atmosphere models are systematically lower than the predicted

---

masses using evolutionary models (the so-called *mass discrepancy* problem, Herrero et al. 1992; Herrero 2003). Fortunately, recent works (Crowther et al. 2002; Herrero et al. 2002; Bianchi & Garcia 2002; Martins et al. 2002) using line-blanketed atmosphere models and accounting both for the spherical stellar atmosphere and for the stellar winds yielded new effective temperature scales for early-type stars and, simultaneously, led to a better agreement between the spectroscopic and evolutionary masses. In this context, the accurate determination of the massive star fundamental parameters, over the whole spectral type and luminosity class range covered by these objects, provides thus the basic material to strengthen our understanding of this particularly important stellar population.

The early-type binary systems are also crucial for the mapping of X-ray emitting plasmas. So far, the most reliable way to constrain the geometry of the hot plasma around stars of various spectral types is through the study of the temporal changes of the X-ray fluxes of eclipsing binaries or rotating stars; the latter only in cases of non-uniform surface distributions of X-ray plasma. A good time coverage of the orbital or rotation cycle is of course critical to provide as complete a description as possible. While late-type stars often experience flaring activities which may considerably complicate the task of mapping their coronae, the situation should, in principle, be much easier in early-type stars. In fact, single early-type objects usually do not display a strong X-ray variability (Berghöfer & Schmitt 1994). In early-type binaries, a significant fraction of the X-ray emission may however arise in a wind interaction zone. The orbital modulation of their X-ray flux is thus quite common, either because of the changing opacity along the line of sight towards the shock region, or as a consequence of the changing properties of the wind interaction zone in an eccentric binary.

In this context, we have undertaken a detailed study of CPD − 41° 7742, a double line spectroscopic binary located in the core of the young open cluster NGC 6231. In Sana et al. (2003, Paper I hereafter), we presented a first accurate orbital solution for the two components of the system. We derived a short period $P = 2.44070$ days and a slight but definite eccentricity $e = 0.027$. Based on spectroscopic criteria, we proposed a spectral type and a luminosity class of O9 III + B1 III for the two components of the system. However we outlined the strong ambiguity concerning the quoted luminosity classification. Indeed the luminosities and radii inferred from the membership in NGC 6231 rather indicate a class V or IV for both components. The analysis of the light curve of the system will allow us to elucidate this question.

We refer to Paper I for a review of the previous works on the object. In Paper I, we dit not mention the work of Balona & Laney (1995) in which the authors present a first light curve of CPD − 41° 7742, showing a clearly-marked eclipse. We also refer to Paper I for details on the spectroscopic analysis of the system. Table 1 summarizes the computed orbital solution and the constraints obtained on its physical parameters. This second paper will complete our current view of the system by providing the analysis of the photometric light curve and of XMM-*Newton* X-ray observations. It is organised as follows. After a description of the optical and X-ray data sets and data handling (Sect. 2), we present the analysis of the

Table 1. Orbital and physical parameters of CPD − 41° 7742 as derived from the He I lines orbital solution presented in Paper I. The usual notations have been adopted. T_0 is the time of periastron passage and is adopted as phase $\psi = 0.0$. The column to the right provides the revised estimate of the errors, obtained with Monte-Carlo simulation techniques (see Sect. 4).

P_{orb} (days)	2.44070	±	0.00050	
e	0.027	±	0.006	0.008
ω (°)	149	±	10	17
T_0 (HJD $-2\,450\,000$)	2400.284	±	0.067	0.113
γ_1 (km s^{-1})	−15.3	±	0.5	1.2
K_1 (km s^{-1})	167.1	±	0.9	1.4
$a_1 \sin i$ ($R_\odot$)	8.05	±	0.05	0.07
γ_2 (km s^{-1})	−26.3	±	0.7	2.4
K_2 (km s^{-1})	301.3	±	1.8	3.0
$a_2 \sin i$ ($R_\odot$)	14.52	±	0.09	0.14
q (=M_1/M_2)	1.803	±	0.015	0.023
$M_1 \sin^3 i$ ($M_\odot$)	16.69	±	0.25	0.39
$M_2 \sin^3 i$ ($M_\odot$)	9.25	±	0.12	0.18

system light curve (Sect. 3). In Sect. 4, we combine the newly obtained information with results from Paper I and we derive the absolute parameters of the system. The X-ray properties of CPD − 41° 7742 are described in Sect. 5. In Sect. 6, we investigate the wind properties and we propose to interpret the X-ray light curve as the signature of a wind interaction. We also present a simple phenomenological model that reproduces reasonably well the observed modulations. Final considerations and conclusions of this work are summarised in Sect. 7.

2. Observations and data reduction

2.1. Photometry

Between 1997 March 22 and April 19, we observed the core of the open cluster NGC 6231 with the 0.6-m Bochum telescope at La Silla, Chile. The Cassegrain focus of the telescope was equipped with a direct camera and a Thomson 7882 charge-coupled device (CCD) detector (384 × 576 pixels) subtending a full field of view of 3.2 by 4.8 arcmin. The photometric observations have been performed through two narrow band filters: one called λ4686 addressing the region of the He II line usually present in massive stars (centre: 4684 Å, *FWHM*: 30 Å) and another one labelled λ6051 addressing a region of the continuum free from strong lines (centre: 6051 Å, *FWHM*: 28 Å). More information on these filters can be found in Royer et al. (1998). The typical exposure times were 60s for both filters. Some 112 (resp. 138) useful frames were obtained with the λ4686 (resp. λ6051) filter. Flat field calibrations were obtained daily on the floodlit dome. No twilight flat could be acquired due to the narrowness of the filters. Several biases were cautiously acquired at various times during the different nights. The frames were debiased using a master zero frame and, in the absence of overscan, a level value interpolated between the various bias frames taken during the same night. The optical elements close to the CCD proved to be frequently contaminated

Table 2. Journal of the photometric observations of CPD − 41° 7742 in the two filters λ6051 and λ4686 (see text). Odd columns give the heliocentric Julian dates (in format HJD − 2 450 000). Even columns provide the observed magnitudes in the selected filter.

		λ6051						λ4686			
HJD	mag	HJD	mag	HJD	mag	HJD	mag	HJD	mag	HJD	mag
530.8192	8.103	540.8836	8.103	549.9225	8.417	534.8722	8.540	545.8333	8.533	554.8312	8.777
530.8203	8.098	540.9142	8.088	550.7756	8.129	534.8968	8.533	545.8758	8.525	554.8680	8.678
531.8341	8.130	540.9223	8.098	550.8198	8.132	535.7976	8.520	545.9226	8.546	554.9149	8.594
531.8354	8.123	540.9286	8.101	550.8595	8.129	535.8262	8.526	546.7415	8.521	555.7662	8.569
533.8018	8.123	541.7697	8.106	550.8872	8.125	535.8670	8.534	546.7979	8.516	555.8110	8.574
533.8033	8.127	541.7939	8.105	550.9163	8.139	535.9103	8.530	546.8556	8.522	555.8573	8.643
533.8041	8.126	541.8431	8.108	550.9216	8.148	537.7754	8.690	546.9197	8.527	555.9148	8.726
533.8291	8.138	541.8689	8.091	551.7497	8.105	537.8168	8.607	547.7870	8.541	555.9303	8.756
533.8299	8.147	541.8974	8.112	551.7937	8.115	537.8576	8.568	547.8468	8.542	556.7881	8.535
533.8307	8.146	542.7511	8.127	551.8060	8.124	537.8590	8.571	547.8905	8.517	556.8690	8.558
533.8571	8.161	542.7896	8.128	551.8631	8.124	537.9009	8.552	547.9242	8.510	557.7451	8.517
533.8579	8.160	542.8192	8.141	551.9181	8.100	538.7595	8.614	548.7645	8.692	557.7899	8.525
533.8587	8.151	542.8482	8.118	552.7605	8.113	538.8022	8.674	548.8095	8.614	557.8334	8.525
533.8823	8.198	542.8906	8.126	552.8081	8.117	538.8615	8.755	548.8509	8.565	557.8599	8.509
533.8831	8.188	543.7525	8.342	552.8566	8.105	538.9045	8.772	548.8781	8.544	557.9078	8.506
533.8839	8.194	543.8084	8.356	552.8789	8.093	539.7730	8.560	548.9168	8.538	557.9249	8.511
533.9053	8.234	543.8701	8.292	552.8798	8.093	539.8246	8.552	548.9212	8.538	558.6961	8.545
533.9063	8.236	543.8955	8.242	552.9189	8.090	539.8655	8.560	549.7466	8.710	558.7425	8.543
533.9270	8.273	543.9226	8.199	553.7507	8.118	539.8983	8.569	549.8067	8.858	558.7897	8.521
533.9278	8.263	544.7848	8.159	553.7947	8.124	540.7890	8.514	549.8637	8.902	558.8082	8.543
533.9286	8.267	544.8474	8.255	553.8328	8.116	540.8306	8.516	549.9214	8.824		
533.9294	8.266	544.8936	8.374	553.8736	8.114	540.8815	8.523	550.7748	8.534		
533.9302	8.274	544.9210	8.442	553.9195	8.111	540.9135	8.531	550.8190	8.531		
534.7974	8.123	544.9281	8.457	554.7069	8.470	540.9217	8.547	550.8586	8.537		
534.8227	8.129	545.7752	8.112	554.7540	8.485	540.9280	8.542	550.8864	8.524		
534.8456	8.130	545.8341	8.119	554.7937	8.430	541.7689	8.523	550.9155	8.546		
534.8730	8.142	545.8766	8.123	554.8319	8.343	541.7931	8.534	550.9208	8.561		
534.8976	8.132	545.9234	8.128	554.8686	8.253	541.8423	8.532	551.7489	8.528		
535.7984	8.118	546.7423	8.100	554.9156	8.168	541.8681	8.523	551.7930	8.535		
535.8270	8.118	546.7987	8.097	555.7669	8.148	541.8966	8.538	551.8052	8.528		
535.8678	8.124	546.8564	8.095	555.8117	8.168	542.7503	8.546	551.8623	8.535		
535.9111	8.110	546.9205	8.109	555.8581	8.228	542.7888	8.542	551.9173	8.519		
537.7762	8.275	547.7881	8.108	555.9156	8.310	542.8183	8.569	552.7569	8.542		
537.8176	8.195	547.8476	8.109	555.9311	8.342	542.8474	8.535	552.7614	8.540		
537.8601	8.157	547.8913	8.086	556.7887	8.135	542.8898	8.546	552.8074	8.528		
537.9021	8.145	547.9250	8.092	556.8698	8.138	543.7516	8.769	552.8551	8.530		
538.7603	8.186	548.7674	8.255	557.7458	8.106	543.8076	8.765	552.8782	8.521		
538.8030	8.258	548.8105	8.184	557.7907	8.095	543.8693	8.701	552.9174	8.522		
538.8623	8.328	548.8519	8.140	557.8342	8.087	543.8947	8.657	553.7500	8.557		
538.9053	8.342	548.8789	8.115	557.8607	8.082	543.9218	8.623	553.7941	8.556		
539.7738	8.137	548.9179	8.115	557.9094	8.079	544.7840	8.560	553.8321	8.540		
539.8254	8.132	548.9200	8.119	557.9257	8.087	544.8465	8.672	553.8729	8.554		
539.8663	8.140	548.9223	8.113	558.6969	8.127	544.8928	8.784	553.9188	8.550		
539.8991	8.142	549.7474	8.302	558.7433	8.103	544.9202	8.858	554.7062	8.887		
540.7898	8.096	549.8075	8.449	558.7910	8.099	544.9272	8.863	554.7533	8.914		
540.8314	8.101	549.8645	8.490	558.8091	8.113	545.7744	8.530	554.7928	8.840		

by dust. Hence, the pixel-to-pixel (high spatial frequency) part of the flat-field calibration had to be carefully extracted from the calibration frames obtained daily. The large scale component of the dome flat fields varied slightly from day to day. This was found to be due to minor changes in the instrumental setup. Night sky superflats proved to be more stable, but yielded a strong systematic vignetting as shown by Manfroid et al. (2001). Consequently, the illumination correction was entirely obtained from the "photometric superflats" based on stellar measurements (see e.g. Manfroid 1995). All reductions were carried out with the National Optical Astronomy Observatories (NOAO) IRAF package. The debiased, flat-fielded frames were analyzed with the DAOPHOT software (Stetson 1987), using aperture radii between 2 and 5.5 arcsec. "Absolute" photometry was derived from the large aperture data, using a multi-night, multi-filter algorithm and a few standard stars (Manfroid 1993). This procedure yielded additional reference stars for each field. These secondary standards together with all non-variable stars
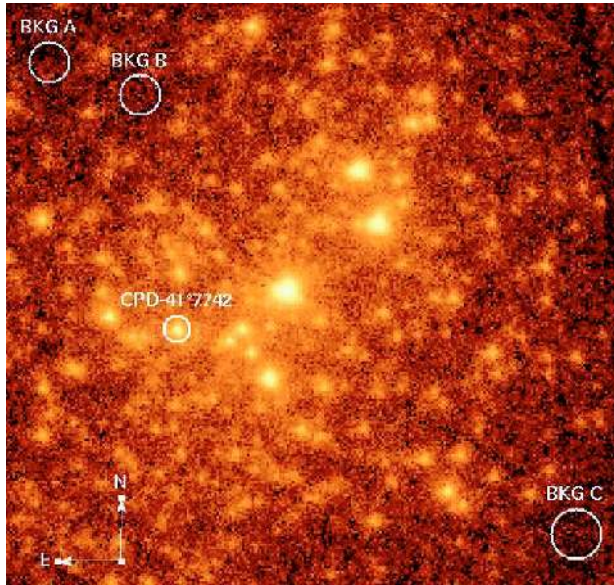
Fig. 1. Broad-band [0.5–10.0 keV] image of the NGC 6231 core. This EPIC MOS1+MOS2 image combines the two instruments and the six pointings of the campaign for a cumulated effective exposure time of 351.5 ks. The source and background extraction regions are shown.

were used to fix, through a global minimization procedure, the zero points for the individual frames and for each aperture radius, thus performing some kind of global differential photometry.

Comparing the photometry performed through the different apertures, we noted that a faint companion visible at 3–4″ to the W-SW of CPD − 41° 7742 has actually no influence on the differential photometry. The final magnitudes are given in Table 2 and correspond to a 2″.5 radius aperture. The expected error on a star of similar brightness as CPD − 41° 7742 corresponds to $\sigma = 0.007$ mag in differential photometry.

2.2. X-ray observation

CPD − 41° 7742 was observed with XMM-*Newton* (Jansen et al. 2001) during the six pointings of the campaign towards NGC 6231 (Sana et al. 2004, 2005a) performed within the guaranteed time programme of the Optical Monitor consortium. The MOS cameras (Turner et al. 2001) were operated in the full frame mode and using the thick filter to avoid contamination by UV/optical light. No EPIC pn data were collected for CPD − 41° 7742 since the star fell on a gap of the pn detector. Due to the brightness of the objects in the field of view (FOV), the Optical Monitor was switched off throughout the campaign. The raw data were processed with the Scientific Analysis System (SAS) version 5.4.1. For details on the XMM-*Newton* observations and on the data processing, we refer to the previous work on HD 152248 – the central target of the FOV – by Sana et al. (2004).

For the purpose of scientific analysis, we adopted a circular extraction region with a radius of 13.2 arcsec and centered on CPD − 41° 7742. This radius corresponds to half the distance to the nearest neighbouring X-ray source.

Using the SAS task CALVIEW, we estimated that, at the position of CPD − 41° 7742, the adopted extraction region corresponds to an encircled energy fraction of about 64% and 63% respectively for the MOS1 and MOS2 instruments. Unfortunately, due to the crowded nature of the NGC 6231 cluster core in the X-rays (see Fig. 1), the background could not be evaluated in the immediate vicinity of CPD − 41° 7742, but had to be taken from the very few source free regions in the cluster core. We adopted three circular background regions – labelled A, B and C on Fig. 1 – centered on $(\alpha, \delta) =$ ($16^h54^m31\overset{s}{.}43, -41°45'42\overset{''}{.}2$), ($16^h54^m23\overset{s}{.}28, -41°46'14\overset{''}{.}7$) and ($16^h53^m44\overset{s}{.}12, -41°53'34\overset{''}{.}6$), and with respective radii of 20, 20 and 25 arcsec. These regions are somewhat offset from the source region but all three are located on the same CCD detector (CCD #1) as CPD − 41° 7742.

Using the average count rates in each pointing, we built raw and background-corrected broad-band light curves in the range [0.5–10.0 keV][1]. We also extracted light curves in three different energy bands: a soft (S_X) band [0.5–1.0 keV], a medium (M_X) band [1.0–2.5 keV] and a hard (H_X) band [2.5–10.0 keV]. For comparison, we used the background corrected count rates in each pointing as given in the cluster X-ray source catalogue. These latter values were obtained by means of a psf-model fit to the source using the SAS task *emldetect* and a spline background function (see details in Sana et al. 2005a). While the catalogue count rates turn out to be about 50% larger than the extracted count rates, both are in excellent agreement when the latter are corrected for the encircled energy fraction. The obtained X-ray light curves show clear variability. To increase our time resolution, we extracted light curves with temporal bins of 5 ks, over the same energy ranges as stated above. The latter curves were corrected for the various good time intervals that result from the data processing; they will be discussed in Sect. 5.

Finally, adopting the same source and background regions, we extracted X-ray spectra for each observation and for each of the two MOS instruments. For this purpose, we used the redistribution matrix files (*rmf*) provided by the XMM-*Newton* instrument teams and we built the appropriate ancillary response files (*arf*) with the help of the SAS software. The spectra were binned in such a way as to have at least 10 counts per energy bin. Using the BLANKSKY files for the MOS instruments, we extracted the spectra corresponding to the adopted source and background regions. The impact of the offset in the background regions on the background spectrum, and on the instrumental emission lines in particular, was found to be negligible.

3. Optical light curve analysis

Photometric light curves were analysed within the framework of the Roche model for an eccentric orbit, similar to Wilson's (Wilson 1979) model. The algorithm is described in detail by Antokhina (1988, 1996), here we only briefly describe its main features. The computer code allows one to calculate a radial

---

[1] Expressed in pulse-invariant (PI) channel numbers and considering that one PI approximately corresponds to 1 eV, the adopted range is actually PI ∈ [500–10 000].

Table 3. Time and orbital phase (according to the ephemeris of Table 1) at mid-exposure for each XMM-*Newton* observation of CPD − 41° 7742. The other columns yield the count rates (in units of 10^{-3} cnt s^{-1}) over different energy bands (expressed in keV) for the two MOS instruments, as obtained using the SAS task *emldetect* (see details in Sana et al. 2005a). The observations lasted on average for 30 ks (corresponding to a phase interval of 0.14). Note that due to background flares, part of some observations had to be discarded.

Obs. #	JD −2 450 000	ψ	MOS1 [0.5–10.0]	[0.5–1.0]	[1.0–2.5]	[2.5–10.0]	MOS2 [0.5–10.0]	[0.5–1.0]	[1.0–2.5]	[2.5–10.0]
1	2158.214	0.819	16.5 ± 0.9	7.7 ± 0.6	8.7 ± 0.6	0.1 ± 0.1	14.3 ± 0.8	7.7 ± 0.6	6.2 ± 0.5	0.4 ± 0.2
2	2158.931	0.113	29.7 ± 1.5	9.8 ± 0.8	17.0 ± 0.9	2.9 ± 0.5	29.0 ± 1.5	10.1 ± 0.9	16.6 ± 1.1	2.2 ± 0.5
3	2159.796	0.468	22.8 ± 1.0	9.0 ± 0.6	12.2 ± 0.6	1.6 ± 0.3	23.6 ± 1.0	9.2 ± 0.6	13.1 ± 0.8	1.3 ± 0.3
4	2160.925	0.930	19.0 ± 1.0	8.4 ± 0.7	9.5 ± 0.7	1.1 ± 0.3	19.3 ± 1.1	9.3 ± 0.7	9.1 ± 0.7	1.0 ± 0.3
5	2161.774	0.278	19.7 ± 1.0	8.5 ± 0.6	10.0 ± 0.7	1.2 ± 0.3	21.1 ± 1.0	8.1 ± 0.6	11.4 ± 0.7	1.6 ± 0.3
6	2162.726	0.668	18.9 ± 0.9	9.5 ± 0.6	8.9 ± 0.7	0.5 ± 0.2	20.3 ± 1.0	9.2 ± 0.6	10.4 ± 0.7	0.7 ± 0.2

Table 4. Input parameters for the program of synthesis of the light curves.

Parameters	Description
$q = M_1/M_2$	Mass ratio
e	Eccentricity
ω	Longitude of periastron of primary star
F_1, F_2	Ratio of surface rotation rate to synchronous rotation rate for both stars
i	Orbital inclination
μ_1, μ_2	Roche lobe filling coefficients, $\mu = R/R^*$, where R and R^* are the polar radii for partial and complete filling of the critical Roche lobe at periastron position $(0 < \mu \leq 1)$
T_1, T_2	Average effective temperatures of the components
β_1, β_2	Gravity darkening coefficients (the temperature of an elementary surface area $T = T_{1,2} \times (\frac{g}{\langle g \rangle_{1,2}})^{\beta_{1,2}}$, where g and $\langle g \rangle$ are the local and mean gravity accelerations)
$x_{1,2}, y_{1,2}$	Limb darkening coefficients (see the text)
A_1, A_2	Bolometric albedos (coefficients of reprocessing of the emission of a companion by "reflection")
l_3	Third light
$\Delta\phi$	Phase shift between the times of conjunction t_0 and of periastron passage T_0 (Table 1)
t_0	Time of primary eclipse minimum

velocity curve, the monochromatic light curves and absorption line profiles of stars simultaneously, either for a circular or an eccentric orbit. Axial rotation of the stars may be non synchronized with the orbital revolution. Following Wilson (1979), we assumed that the shapes of the stars coincide with equipotential surfaces in the Roche model at all orbital phases and both stars retain constant volumes during their orbital revolution. The tidally distorted surfaces of the stars are heated by mutual radiation. The intensity of the radiation coming from an elementary area of the stellar surface and its angular dependence are determined by the temperature of the star, gravitational darkening, limb darkening, and heating by radiation from the companion. The input parameters of the model are summarized in Table 4.

For light curve solution, we fixed some parameters whose values were defined in previous investigations of the system or can be assumed from global stellar properties. Namely, we used the known spectroscopic value of mass ratio

$q = M_1/M_2 = 1.803$, deduced from the data on He I lines (Paper I). A light curve solution is only sensitive to the temperature ratio between the stars, thus the temperature of one star should be fixed. Usually it is the more reliably determined temperature of the primary star. The spectral types of the stars O9 III (primary) and B1 III (secondary) were derived in Paper I, but we pointed out that adopting a main sequence luminosity class for both components solves much of the inconsistency between the luminosity class III hypothesis and the typical luminosities and radii of giant stars. Our preliminary light curve solution resulted in stellar radii also suggesting the luminosity class V for both stars, thus we fixed the average effective temperature of the primary $T_1 = 34\,000$ K corresponding to an O9 V star (Humphreys & McElroy 1984). This value is also very close to the one given by the new effective temperature scale of O-type dwarfs by Martins et al. (2002).

Gravity-darkening coefficients $\beta_1 = \beta_2 = 0.25$ and albedos $A_1 = A_2 = 1$ were assumed as typical for early type stars. We used the nonlinear "square-root" limb-darkening law (Diaz-Cordoves & Gimenez 1992; Diaz-Cordoves et al. 1995; van Hamme 1993): $I(\cos\gamma) = I(1)[1 - x(1 - \cos\gamma) - y(1 - \sqrt{\cos\gamma})]$, where γ is the angle between the line of sight and the normal to the surface, $I(1)$ is the intensity for $\gamma = 0$, and x, y are the limb darkening coefficients. As shown by van Hamme (1993), this is the most appropriate limb-darkening law at optical wavelengths for $T \geq 10\,000$ K. The rotation of both stars is assumed to be synchronous with the orbital one $F_1 = F_2 = 1$.

The adjustable parameters of the model were the following: the Roche lobe filling coefficients for the primary and secondary μ_1, μ_2 (calculated for the time of periastron passage), the average effective temperature of the secondary star T_2, the orbital inclination i, the eccentricity e, the longitude of periastron of the primary ω. While doing minimization, every model light curve was also shifted along the magnitude axis until the best fit between the model and the observed curves was achieved.

Initial phases ψ of observational data points were calculated using the spectroscopic ephemeris of Table 1: HJD = $2\,452\,400.284 + 2\overset{d}{.}44070 \times E$. Since our model assumes an orbital phase ϕ equal to zero at the time of conjunction (the secondary star being in front), the observed light curve was then shifted in phase by $\Delta\phi$, according to $\psi = \phi - \Delta\phi$. The value of $\Delta\phi$ was determined by the minimum of the deviation between the observed and model light curves.

Table 5. CPD − 41° 7742 physical and orbital parameters as obtained from the optical light curve analysis. Two kinds of error estimates are given. The first one defines the confidence intervals inside which the model is still accepted at the 1% significance level (see text). The second one (given in brackets) corresponds to the 1-σ intervals used to define the domain where the true parameter values are expected to lie.

Parameters	$\lambda 4686$ Å	$\lambda 6051$ Å	Simultaneous solution	Parameter status
$q = M_1/M_2$	1.803	1.803	1.803	adopted
i	$77°\!.35 \pm 0°\!.05\ (0°\!.8)$	$77°\!.37 \pm 0°\!.05\ (0°\!.8)$	$77°\!.35 \pm 0°\!.05\ (0°\!.8)$	adjusted
e	$0.020 \pm 0.001\ (0.006)$	$0.020 \pm 0.001\ (0.006)$	$0.020 \pm 0.001\ (0.006)$	adjusted
ω	$33° \pm 8°\ (19°)$	$33° \pm 8°\ (19°)$	$33° \pm 8°\ (19°)$	adjusted
μ_1	$0.782 \pm 0.004\ (0.037)$	$0.784 \pm 0.004\ (0.037)$	$0.783 \pm 0.004\ (0.037)$	adjusted
μ_2	$0.748 \pm 0.003\ (0.050)$	$0.751 \pm 0.003\ (0.050)$	$0.749 \pm 0.003\ (0.050)$	adjusted
T_1 (K)	34 000	34 000	34 000	adopted
T_2 (K)	$26\,280 \pm 150\ (420)$	$26\,230 \pm 150\ (420)$	$26\,260 \pm 150\ (420)$	adjusted
$L_1/(L_1 + L_2)$	0.7380	0.7308	0.7379 $\mid$ 0.7314	computed
$L_2/(L_1 + L_2)$	0.2620	0.2692	0.2621 $\mid$ 0.2686	computed
F_1	1.0	1.0	1.0	adopted
F_2	1.0	1.0	1.0	adopted
β_1	0.25	0.25	0.25	adopted
β_2	0.25	0.25	0.25	adopted
A_1	1.0	1.0	1.0	adopted
A_2	1.0	1.0	1.0	adopted
l_3	0.0	0.0	0.0	adopted
x_1	−0.213	−0.188	−0.213 $\mid$ − 0.188	adopted
y_1	0.724	0.643	0.724 $\mid$ 0.643	adopted
x_2	−0.124	−0.112	−0.124 $\mid$ − 0.112	adopted
y_2	0.663	0.559	0.663 $\mid$ 0.559	adopted
$\Delta \phi$	$0.1537 \pm 0.0007\ (0.0011)$	$0.1537 \pm 0.0007\ (0.0011)$	$0.1537 \pm 0.0007\ (0.0011)$	adjusted
t_0 (HJD − 2 450 000)	2399.909	2399.909	2399.909	computed
Relative radii (R/a)				
$r_1(pole)$	$0.3127 \pm 0.0016\ (0.0148)$	$0.3135 \pm 0.0016\ (0.0148)$	$0.3131 \pm 0.0016\ (0.0148)$	
$r_1(point)$	$0.3351 \pm 0.0022\ (0.0203)$	$0.3362 \pm 0.0022\ (0.0203)$	$0.3357 \pm 0.0022\ (0.0203)$	
$r_1(side)$	$0.3205 \pm 0.0018\ (0.0164)$	$0.3214 \pm 0.0018\ (0.0164)$	$0.3210 \pm 0.0018\ (0.0164)$	
$r_1(back)$	$0.3290 \pm 0.0020\ (0.0182)$	$0.3300 \pm 0.0020\ (0.0182)$	$0.3295 \pm 0.0020\ (0.0182)$	
$r_2(pole)$	$0.2268 \pm 0.0009\ (0.0152)$	$0.2277 \pm 0.0009\ (0.0152)$	$0.2271 \pm 0.0009\ (0.0152)$	
$r_2(point)$	$0.2421 \pm 0.0012\ (0.0210)$	$0.2433 \pm 0.0012\ (0.0210)$	$0.2425 \pm 0.0012\ (0.0210)$	
$r_2(side)$	$0.2306 \pm 0.0010\ (0.0163)$	$0.2316 \pm 0.0010\ (0.0163)$	$0.2309 \pm 0.0010\ (0.0163)$	
$r_2(back)$	$0.2384 \pm 0.0011\ (0.0189)$	$0.2395 \pm 0.0011\ (0.0189)$	$0.2387 \pm 0.0011\ (0.0189)$	

The estimation of adjustable parameters was done with the well-known simplex algorithm (Nelder and Mead's method) (Himmelblau 1971; Kallrath & Linnell 1987). In the vicinity of the minima found, additional calculations were done on a fine grid, in order to explore the details in shape of the deviation surface and to estimate the errors on the parameters. The resulting parameters for the solutions corresponding to $\lambda 4686$ Å, to $\lambda 6051$ Å and to the simultaneous adjustment at both wavelengths are presented in Table 5. Two kinds of confidence intervals have been computed and are also given in Table 5. The first one corresponds to a test of the adequacy of the model. The confidence intervals for the parameters are estimated using an absolute critical value of χ^2 corresponding to a significance level of 1%. This first approach rather defines the zones of variation of the parameters that still lead to an acceptation of the model. The obtained error bars are rather small. The second kind of confidence intervals corresponds to a critical value which is defined relatively to the obtained minimum χ^2 of the fit, increased by a value corresponding to a significance level

of 0.1%. This latter interval corresponds to a 3-σ deviation and it has been transformed to a 1σ-uncertainty in the sake of coherence with the radial velocity adjustment. This approach is reminiscent to a search for the zone where lie the true values of the parameters.

Figure 2 exhibits the observed light curves corresponding to $\lambda 4686$ Å and to $\lambda 6051$ Å along with the model predictions of the simultaneous solution. The final model for CPD − 41° 7742 viewed at different orbital phases is presented in Fig. 3.

4. CPD − 41° 7742 orbital and physical parameters

4.1. Period P

Since the time base of our photometric campaign is *only* 28 days long, it provides little constraint on the period. Indeed the width of the associated peak in the periodogram is about $3.6 \times 10^{-2}\,\mathrm{d}^{-1}$, yielding an uncertainty of about $2.1 \times 10^{-2}\,\mathrm{d}$ (corresponding to one tenth of the peak width) on the value of a period determined from the photometric set only. As a
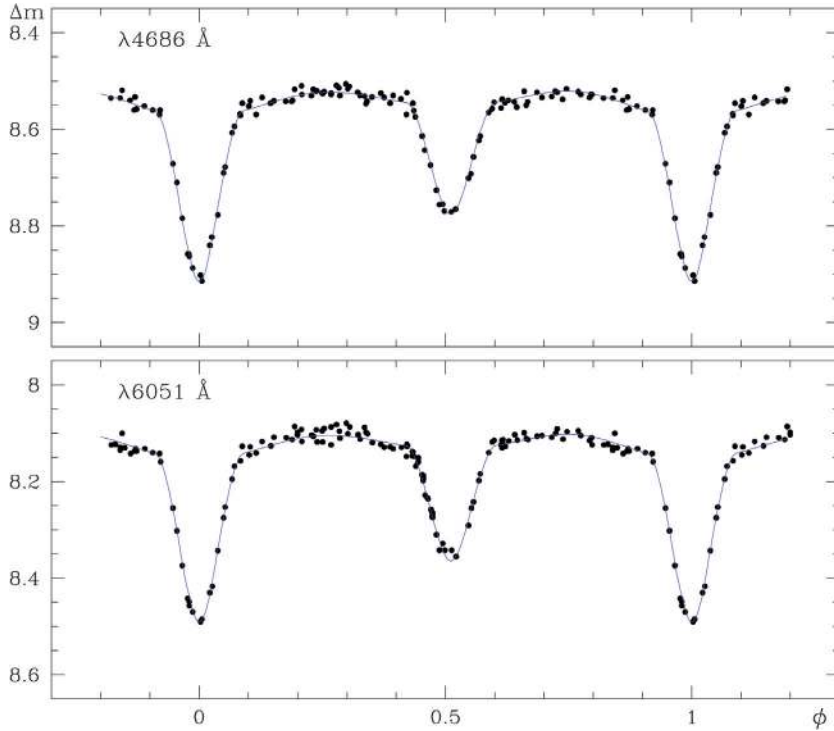
Fig. 2. Observed (dots) and modelled (plain lines) light curves at $\lambda 4686$ Å and $\lambda 6051$ Å. The parameters of the adopted model are presented in Table 5. The minimum of the primary eclipse is adopted as phase $\phi = 0.0$ which, according to the ephemeris of Table 1, corresponds to $\psi \approx 0.85$.

consequence, we choose to keep the period fixed at the value determined from the much longer time span of our spectroscopic data set. We thus retain $P = 2.44070$ d for CPD − 41° 7742.

4.2. Eccentricity e

The values of the eccentricity obtained from the analysis of the light curve and of the radial velocity curve are in excellent agreement. From our data, the separation between the two light minima is indeed clearly different from half an orbital cycle and the CPD − 41° 7742 orbit is thus slightly eccentric.

Recently, Sterken & Bouzid (2004) led a photometric campaign searching for new variables in NGC 6231. Using the period from Paper I, they obtained independent light curves for CPD − 41° 7742 in the Strömgren system. Surprisingly, their data set reveals almost perfectly symmetric light curves with the two light minima separated by exactly half a cycle, thus indicating either a non eccentric system or a longitude of periastron very close to 90 or 270°. No detailed analysis of the light curve has been published yet, but the differences between the Sterken & Bouzid observations and ours are quite intriguing.

In our data, the ingress of the secondary eclipse has been observed during three different nights spread over the one month run. It is therefore well defined and clearly indicates a slight eccentricity, except if some systematic biases were present. Our observing run lasted for 28 days and the CPD − 41° 7742 light curves displayed in Fig. 2 show smooth ellipsoidal variations and well behaved eclipses. Spread over at least two years and acquired more recently,

the Sterken & Bouzid data set is larger, especially in the y and b bands, though with some gaps in the phase coverage. Their published light curves display several striking features. First, the primary eclipse seems to vary over the time: it presents different depths over different cycles and shows different ingress and egress shapes. Rapid variations are also observed slightly before the primary eclipse as well as slightly after the secondary one. The right wing of the secondary eclipse displays an inflection point in the y and b bands, while a strange *bifurcation* is observed in the u band. Finally, even outside the eclipses, the behaviour of the system is clearly not as quiet as in our data set (see Fig. 2).

While a change of the period or of the eccentricity with time is hard to explain, a change in the longitude of the periastron could mimic a non-eccentric system. Another hypothesis, also mentioned by Sterken & Bouzid, is that the observed dispersion of their light curves reveal the signature of some kind of activity in CPD − 41° 7742. Under this hypothesis, the system could have remained in a quiet state during the 11-cycle duration of our observations, while Sterken & Bouzid could have observed different activity states during the longer time-span of their campaign.

4.3. Longitude of periastron ω

The two values for the primary longitude of periastron obtained from the spectroscopy ($\omega = 149°$) and from the photometry ($\omega = 33°$) are clearly not consistent. In Paper I, we also computed an orbital solution including all published primary RVs and we obtained an argument $\omega = 27 \pm 31°$ closer to the

Table 6. CPD − 41° 7742 absolute parameters. The errors on the luminosities and the magnitudes were estimated assuming a formal error of 1000 K on the temperatures.

Parameters	Primary	Secondary
$a(R_\odot)$	23.18 ± 0.18	
$R(R_\odot)$	7.45 ± 0.45	5.39 ± 0.43
$M(M_\odot)$	17.97 ± 0.45	9.96 ± 0.22
T(K)	$34\,000$	$26\,260$
$\log(L_{\rm bol}/L_\odot)$	4.82 ± 0.07	4.09 ± 0.10
$\log(g)$	3.93 ± 0.48	3.96 ± 0.64
$M_{\rm V}$	-4.00 ± 0.21	-2.98 ± 0.31

latter photometric value. In principle, the light curve analysis is a more powerful tool to derive accurate values for ω, again from the separation between the two light minima. In Fig. 2, the separation between the primary and secondary eclipses is slightly larger than half a cycle. This indicates that the longitude of periastron is located between 0° and 90°, thus rejecting the much larger spectroscopic value.

In Paper I, we already noted the large dispersion in the values deduced from data sets associated with different lines, ranging from $\omega = 99°$ to 190°. We tentatively suggested that this was linked to the difficulty to accurately determine the periastron argument in such a slightly eccentric system. From our orbital solution, we however derived a reasonable error bar of 10°. While searching for the origin of the discrepancy between the photometric and spectroscopic solutions, we have investigated this point more deeply. Adopting the orbital parameters of Table 1, we computed a set of orbital solutions, varying the periastron argument from 0° to 360°. The obtained curves are very similar in shape; the main difference is a shift in radial velocity of an amplitude of about $10\,{\rm km\,s^{-1}}$ peak-to-peak. Comparing this with the root-mean-square (rms) residual of $4.8\,{\rm km\,s^{-1}}$ of our orbital solution gives us a first impression that the periastron argument is probably loosely constrained by the radial velocity solution and that the quoted error-bar could be underestimated in this particular case.

In a second approach, we performed Monte-Carlo simulations adopting a Gaussian distribution of the errors on the measured radial velocities (RVs). For the primary, we adopted a standard deviation of $4.8\,{\rm km\,s^{-1}}$, thus equal to the rms residual of our fit. For the secondary component, we accounted for the obtained ratio between the primary and secondary uncertainties, $s_y/s_x = 2.1$, as quoted in Paper I. Finally, for each observation, we scaled the dispersion according to the relative weighting adopted to compute the orbital solution. For each measured RVs, we randomly drew a series of 10 000 simulated RV points from these distributions, so building an equivalent number of simulated data sets. We then computed the corresponding orbital solutions using the same method as the one described in Paper I. We finally computed the distributions of the resulting orbital elements. This latter approach allows to estimate the errors assuming a random dispersion of the observed points. This evidently does not account for possible systematic errors or outstanding points.
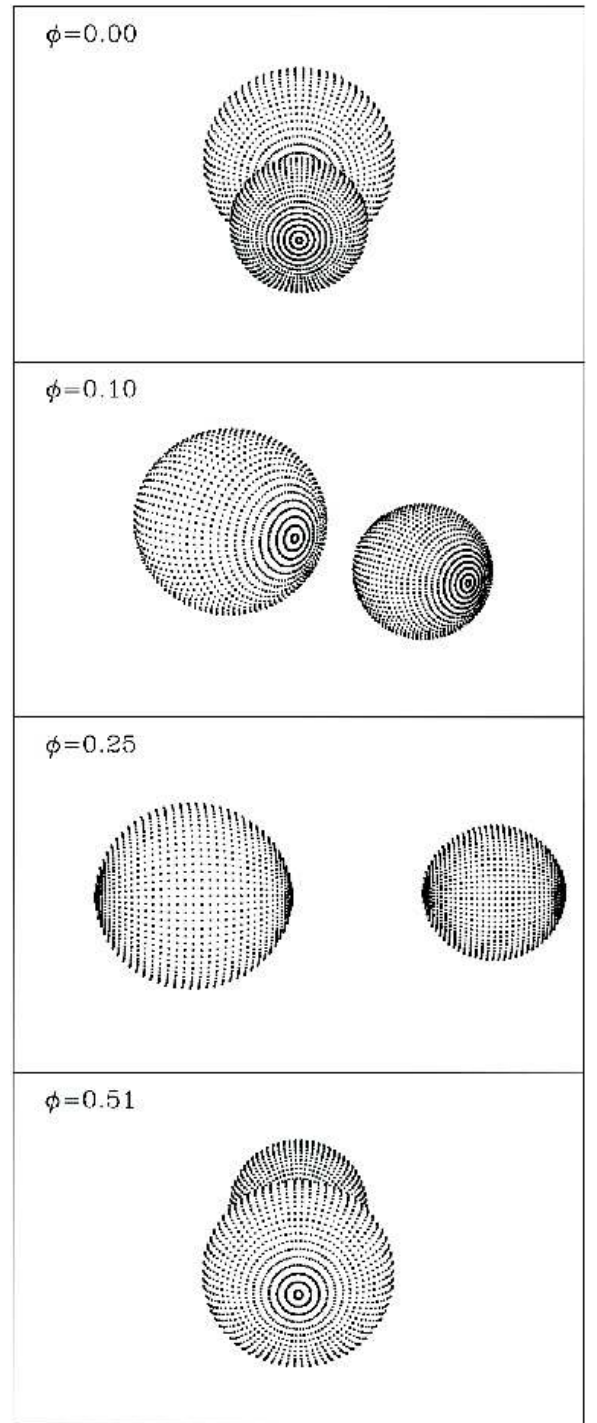

Fig. 3. The model of CPD − 41° 7742 viewed at different orbital phases ϕ. The corresponding phases using the ephemeris of Table 1 are, from top to bottom, $\psi = 0.85$, 0.95, 0.10 and 0.36.

We found that all the orbital parameters follow a Gaussian distribution, centered on the values of Table 1, except the longitude of periastron (and thus the time of periastron passage). The simulated 1-σ dispersions were found to be systematically, but not dramatically, higher than the published uncertainties. The difference is, on average, not larger than 80% but can reach a factor of 3. These new values for the uncertainties are quoted in the right column of Table 1. Concerning the distribution
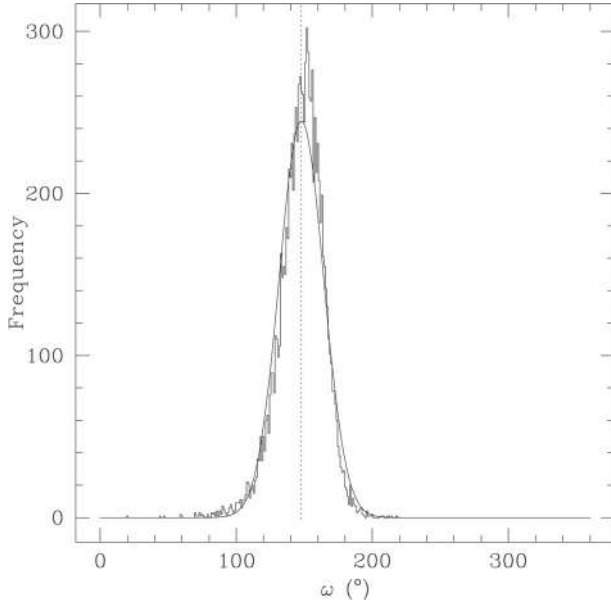
Fig. 4. Distribution of the longitude of periastron ω in a set of 10 000 simulated orbital solutions built using Monte-Carlo techniques (see text). An equivalent Gaussian characterized by the same estimated mean and standard dispersion and with an equivalent surface has been overplotted.

of the periastron argument, Fig. 4 shows that it significantly deviates from a Gaussian distribution. The width of the peak however does approximately correspond to the width of an equivalent Gaussian characterized by an estimated standard deviation equal to the one of the simulated distribution and by an equivalent surface. We thus retain the 1-σ dispersion of the distribution as a good estimator of the typical error on the determined spectroscopic value for ω. As a consequence, while the quoted error on the periastron argument was indeed underestimated in Paper I, this new estimate explains rather well the dispersion observed from time to time but still rules out the photometric value $\omega = 33°$. The origin of the inconsistency between the photometric and spectroscopic values, as well as with the Sterken & Bouzid (2004) data, should be looked for elsewhere.

One could indeed think of a possible physical effect that would modify the observed RV curve compared to the *true* curve of the system. In particular, a modification of the position of the spectral line centroids could produce a different RV value compared to the *true* velocity of the stars. In such a slightly eccentric binary as CPD − 41° 7742, it is also plausible that a small variation in the measured RVs could mimic orbits with quite a different periastron argument. Though the exact nature of the phenomenon is unknown, we tentatively linked it to a possible manifestation of the Barr effect.

The Canadian amateur astronomer, J. Miller Barr noted that the longitudes of periastron of spectroscopic binaries are not uniformly distributed between 0° and 360° (Barr 1908). Out of 30 spectroscopic binaries with elliptical orbits, apparently only four had ω between 180° and 360°, all others had their longitude of periastron in the first two quadrants. Barr advanced two possible explanations for this systematic effect: either the

pressure or temperature effects in the atmospheres of the stars shift their spectral lines with respect to their genuine orbital motion, or a non-uniform brightness of the components combined with a large rotational velocity causes the spectral lines to become asymmetric. Although Barr included several Cepheid variables in his sample, a similar effect was (re-)discovered by Struve (1948, see also the discussion by Batten 1983, 1988). Struve apparently found an excess of systems with ω in the first quadrant. He suggested that this could be due to streams of gas between the stars which lead to spurious eccentricities and values of ω in the first quadrant. The existence of the Barr effect was confirmed by the studies of Fracastoro (1979) and Howarth (1993). Fracastoro used the data from the VIIth Catalogue of orbital elements of spectroscopic binaries and found a distribution of ω for systems with large eccentricities ($e \geq 0.6$) that shows an excess of systems with $\omega = 0°$ and a flat minimum around $\omega = 250°$. The effect was most prominent in systems with short orbital periods. Howarth (1993) analysed the effect by means of non-parametric statistical tests, restricting his sample to systems with orbital solutions of reasonable quality. He found a statistically significant effect only for systems with orbital periods shorter than 3 days. The distribution of ω peaks at a preferred direction of $\omega \simeq 100°$, corresponding to a shallower, longer rising branch in the radial velocity curve and a steeper, shorter falling branch. Howarth interpreted this effect as the result of a gas stream from the primary towards the secondary, though no simulation of the phenomenon has been performed to check its exact influence on the RV curve.

4.4. Time of periastron passage T_0

The difference in the spectroscopically and photometrically determined times of periastron passage directly results from the inconsistency between the values of the periastron argument derived using the two techniques. This problem has already been extensively described in the previous paragraph (Sect. 4.3). We just note here that adopting a periastron argument $\omega = 33°$ yields a value for the time of periastron passage of $T_0 = 2\,452\,399.498$ (HJD).

4.5. CPD − 41° 7742 physical parameters

Thanks to the light curve analysis, the inclination of the system is now very well constrained. Combining this with the spectroscopic information of Table 1, we derived absolute values for the system separation and the star radii and masses. We also derived their luminosity and the surface gravity. The physical parameters of both stars are given in Table 6. With an absolute radius of $R_1 = 7.45 \pm 0.45\,R_\odot$, the primary component is slightly smaller than typical O9 V stars. Howarth & Prinja (1989), Schmidt-Kaler (1982) and Vacca et al. (1996) respectively listed radii of 8, 9.5 and 8.8 $R_\odot$. The observed radius is however larger than the typical O9.5 V radius of 7 $R_\odot$ given by Howarth & Prinja. Adopting the bolometric correction of Humphreys & McElroy, $BC = -3.3 \pm 0.1$, we derived a visual absolute magnitude $M_{V,1} = -4.00 \pm 0.21$, fainter than the values of −4.5, −4.2, −4.5 and −4.43 respectively reported
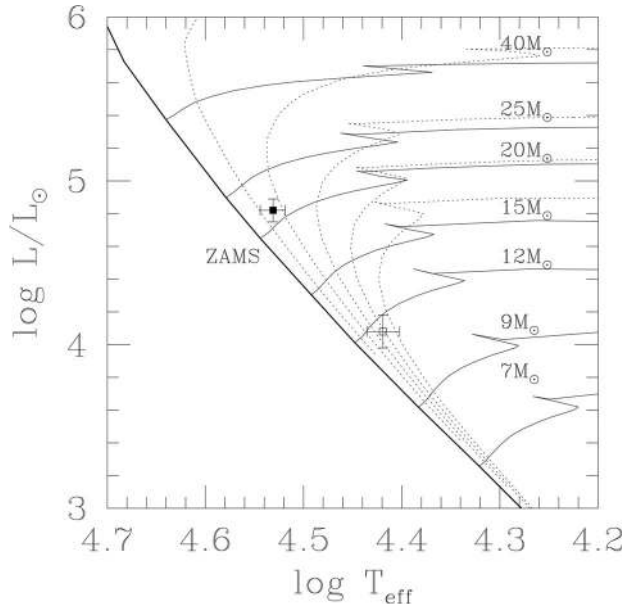
Fig. 5. Position of the primary (filled symbol) and secondary (open symbol) components of CPD − 41° 7742 in the H-R diagram. A formal error of 1000 K has been adopted on the temperatures. Solid lines: evolutionary tracks from Schaller et al. (1992) for different initial masses. Dotted lines: isochrones ranging, from left to right, from 2 to 10 Myr with a step of 2 Myr.

Fig. 6. Net EPIC MOS count rates of CPD − 41° 7742 as a function of orbital phase and averaged over the duration of each pointing (from Sana et al. 2005a). The vertical axes are in units 10^{-3} cnt s^{-1}. The horizontal *error bars* indicate the extension in phase of the corresponding pointing.

by Humphreys & McElroy (1984), Howarth & Prinja (1989), Schmidt-Kaler (1982) and Vacca et al. (1996), though again in agreement with the slightly later spectral-type O9.5 V. Comparing the obtained values with those of other eclipsing early-type binaries listed by Gies (2003) clearly indicates that the physical parameters of the primary in CPD − 41° 7742 correspond to the observed range for O9 dwarfs. Vaz et al. (1997) reported a mass of 19 $M_\odot$ for the O9 V component in HD 165921 though with a relatively smaller radius ($R = 6.13\ R_\odot$). On the other hand, the CPD − 41° 7742 primary is slightly larger and heavier than the O9.5 dwarf components in CPD−59°2603 (Rauw et al. 2001, $M = 14.5\ M_\odot$, $R = 4.9\ R_\odot$), HD 193611 (Popper & Hill 1991, $M = 16.6 + 16.3\ M_\odot$, $R = 7.4 + 7.4\ R_\odot$) or HD 198846 (Simon et al. 1994; Hill & Holmgren 1995; Burkholder et al. 1997, $M = 17.0 − 17.7\ M_\odot$, $R = 5.7 − 7.7\ R_\odot$). The dwarf nature of the primary star is consistent with the derived surface gravity (although the corresponding error is rather large).

From the effective temperature calibration of Humphreys & McElroy, the secondary temperature corresponds to a spectral sub-type B0.5, in rough agreement with the B1 spectral type obtained from spectroscopy. Its radius and visual magnitude however fall within the expected range for B1–2 stars (Humphreys & McElroy 1984; Schmidt-Kaler 1982). The secondary is also slightly smaller and lighter than the B1 V component in HD 175514 (Bell et al. 1987, $M = 13.5\ M_\odot$, $R = 5.9\ R_\odot$). All in all, and accounting for the uncertainties on the spectroscopic data, adopting a B1.5 V spectral sub-type for the secondary in CPD − 41° 7742 yields a better match between its physical parameters and the typical observed and theoretical values expected for such a star.
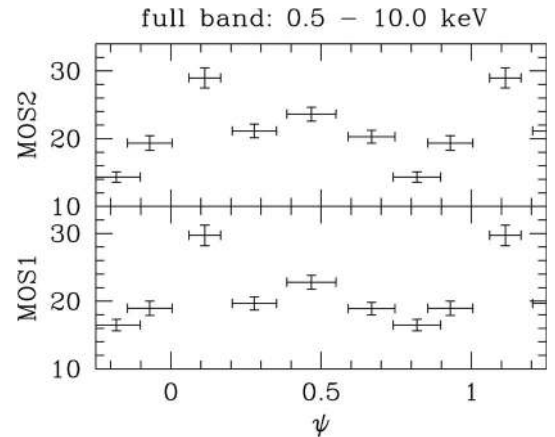
The locations of the CPD − 41° 7742 components in the H-R diagram are shown in Fig. 5 together with the evolutionary tracks of Schaller et al. (1992). A rough interpolation from these tracks yields initial masses $M_1^{(0)} = 23.7\ M_\odot$ and $M_2^{(0)} = 11.1\ M_\odot$ and current ages between 3 and 8 Myr. These ages do well reproduce the range of derived values for the NGC 6231 cluster (see the cluster literature review in Sana et al. 2005a). In such a small time span, the actual masses of the stars remain close to their initial masses and are thus quite larger than the observed masses of about 18 and 10 $M_\odot$ (Table 6). In a binary system, mass exchange between its components, through e.g. Roche lobe overflow, could alter their evolutionary status compared to single star models. From the photometric light curve, CPD − 41° 7742 is actually a well detached system. Due to its young age, it is thus very unlikely that the system could have undergone such a phenomenon (now interrupted) in its past history. New evolutionary tracks that account for the effect of rotation could help to investigate this apparent discrepancy. Finally, comparing the absolute magnitudes obtained in Table 6 with the visual magnitude $V = 8.228$ of CPD − 41° 7742 (Sung et al. 1998), we estimated the distance of the object. We adopted a colour excess $E(B − V) = 0.49$ and $R = 3.3$ as derived by Sung et al. (1998). We finally obtained $DM = 10.92 \pm 0.16$, in excellent agreement with the cluster average distance modulus $DM = 11.07 \pm 0.04$ (Sana et al. 2005a).

5. X-ray light curves and spectral analysis

The X-ray light curves of CPD − 41° 7742 as seen by the two MOS cameras are shown in Fig. 6. The count rates, averaged over the duration of each pointing, were taken from the NGC 6231 X-ray source catalogue of Sana et al. (2005a) and were obtained using the SAS task *emldetect*. The count rates are thus corrected for the effects of exposure, vignetting and finite size of the extraction region. They also account for the background subtraction. It is clear from Fig. 6 that the X-ray emission from CPD − 41° 7742 displays strong signs of variability. A χ^2 test of hypothesis consistently rejects, at the 1%
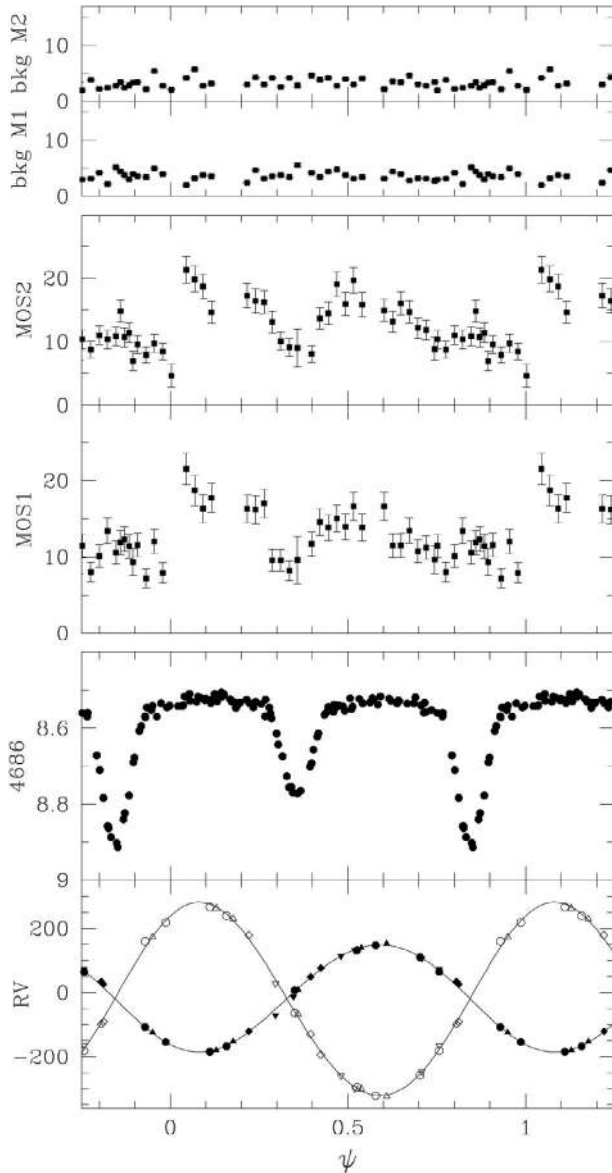
Fig. 7. *Top panel*: EPIC MOS background count rates in the [0.5–10.0 keV] band. *Middle panel*: CPD − 41° 7742 EPIC MOS background-corrected count rates in the same energy range. The time binning of these two panels is 5 ks. The vertical axes are in units 10^{-3} cnt s^{-1}. No correction for the limited encircled energy fraction has been applied. *Lower panel*: RV curve (in km s^{-1}) and optical light curve (in mag) of CPD − 41° 7742. Note the coincidence of the X-ray drop around $\psi = 0.35$ and the time of conjunction with the primary star being in front, as well as the lack of coincidence of the secondary eclipse with the passage at the systemic velocity.

significance level, the null hypothesis of constant rates in the [0.5–10.0 keV] band and in the M_X and H_X bands. Figure 6 also indicates that the phase coverage of the orbital cycle is almost complete with only a small gap slightly before phase $\psi = 0.2$. To increase our time resolution, we also extracted background-corrected light curves with a time binning of 5 ks. Figure 7 shows that the count rate changes by about a factor two over relatively short time scales. These variations are also seen in the different energy ranges (Fig. 8) and are most prominent in the intermediate (M_X) band. As in Fig. 7, they suggest

a double-peaked light curve with two broad maxima around phases $\psi \approx 0.1$ and 0.5. From the top panels of Fig. 7, we conclude that the observed modulations are clearly not due to background fluctuations. Note that, in Figs. 7 and 8, no correction for the limited encircled energy fraction has been applied, neither for the vignetting nor for the exposure. This explains the lower count rates obtained compared to Fig. 6.

One of the main pictures in the X-ray light curve is a sensible decrease of the signal between phase $\psi = 0.27$ and 0.45, which almost exactly corresponds to the time of the secondary minimum in the optical light curve. The observed modulations are probably phase-locked since, for example, the two wings of the *eclipse* have been observed during two different orbital revolutions. However, except near $\psi = 0.85$, the different pointings do not overlap in phase. One can therefore not definitively assert the phase-locked behaviour of the observed X-ray light curves.

Figure 7 seems thus to indicate two different emission levels: a higher state between $\psi \approx 0.0$ and 0.5, during which the *eclipse* is observed, and a lower state between $\psi \approx 0.6$ and 1.0, where no counterpart of the primary eclipse can be seen. The hardness ratio curves are shown in Fig. 9. Though the error bars are quite large, they seem to indicate that the emission is slightly softer around phase $\psi = 0.3$, so approximately at the time of conjunction, while it is presumably harder at the maximum of the emission.

While the orbit is presumably not circular, the value of the eccentricity is pretty small and it is unlikely that the variation of the distance between the two stars plays a significant role in CPD − 41° 7742. In consequence, the observed modulations of the X-ray emission are more probably due to a modification of the line of sight towards the system while it is revolving around its center of mass. The observed X-ray light curves will be discussed in the framework of a wind interaction model presented in the next section (Sect. 6.3).

As a next step in the analysis, we attempt to constrain the physical properties of the X-ray emission by adjusting a series of models to the obtained spectra for each pointing. We simultaneously fitted the two MOS spectra using the XSPEC software v.11.2.0 (Arnaud 1996). Using the $B − V$ colours quoted by Baume et al. (1999) and Sung et al. (1998), we infer a colour excess of about $E(B − V) = 0.49$ for CPD − 41° 7742. The corresponding ISM neutral hydrogen column density amounts to $N_H^{ISM} = 2.8 \times 10^{21}$ cm^{-2}. In the spectral fits, we thus requested a column density larger or equal to N_H^{ISM}. The best spectral fits are obtained for a two-temperature mekal thermal plasma model (Mewe et al. 1985; Kaastra 1992) with two independent absorbing columns. These fits indicate a soft ($kT \sim 0.6$ keV) slightly absorbed plus a harder ($kT \sim 1.0$ keV) and more heavily absorbed component. However, they only provide an upper limit on the absorbing column associated to the soft component. As for HD 152248 (Sana et al. 2004), fixing this additional soft column to zero yields even better fits, characterized by more stable solutions. The best-fit parameters are listed in Table 7 and tend to indicate that the CPD − 41° 7742 X-ray spectrum is significantly harder when the total flux is larger. More accurate information is however difficult to obtain since, as can be deduced from the modulations of the hardness
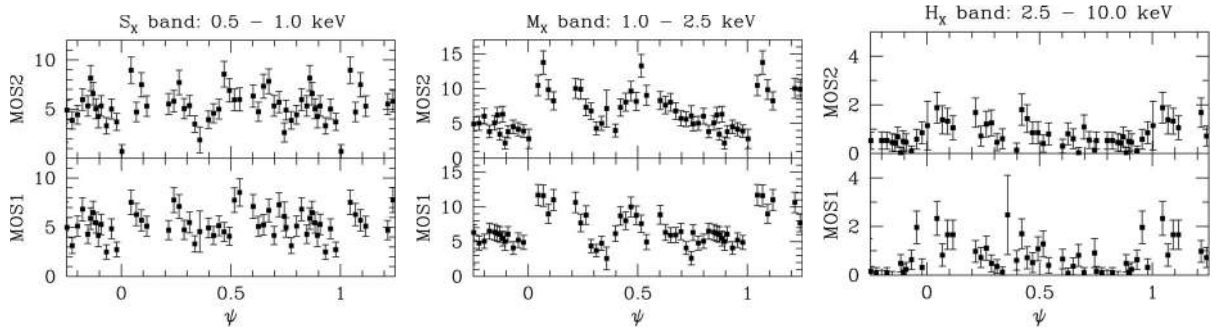
Fig. 8. CPD – 41° 7742 EPIC MOS background-corrected count rates in the three energy bands as a function of orbital phase. The time binning is 5 ks. The vertical axes are in units 10^{-3} cnt s^{-1}. No correction for the limited encircled energy fraction has been applied.
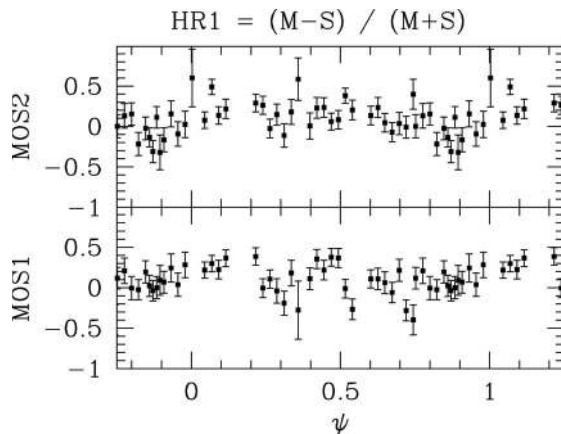

Fig. 9. Hardness ratios vs. phase for the EPIC MOS instruments. The adopted definition for HR_1 is given on top of the panel.

ratios (Fig. 9), the spectral variations are probably averaged out over the 30 ks duration of a pointing. Unfortunately, smaller bin sizes do not allow to obtain spectra of a sufficient quality to derive reliable constraints on the spectral properties.

The combined MOS spectra obtained from the merging of the six XMM-*Newton* observations are shown in Fig. 10 together with the best fit 2-T model. Though the general quality of the fit is relatively good, the model tends to underestimate the fluxes at high energy (>4 keV). This could indicate the existence of a high energy component as well as the presence of the Fe K line at 6.7 keV. The merged spectra do unfortunately not have a sufficient quality at high energy to constrain this probable additional component.

6. CPD – 41° 7742 X-ray properties

6.1. X-ray emission from the stellar components

The X-ray emission from massive stars presumably comes from shell collisions within the lower layers of their winds, which result from the growing of radiatively-driven wind instabilities (Feldmeier et al. 1997). It is expected that the bulk of the emission is produced in a zone extending to about five times the stellar radius. Within a binary system with an inclination close to 90°, we thus expect only a small fraction of this extended emission zone to be occulted by the motion of one companion in front of the other. In consequence, because of the much larger emission zone, the eclipses in the X-ray domain are probably not as clearly marked as in the optical.

However, the CPD – 41° 7742 X-ray light curve (Fig. 7) shows a clear decrease – around $\psi = 0.35$ – almost perfectly synchronized with the optical secondary eclipse. This suggests a different geometry and, probably, the presence of a localized emission component, in addition to the intrinsic emission of the two stars. To match the observed light curve, this component should be occulted around $\psi = 0.35$. It should thus be associated either with the primary inner side, or with the secondary inner or outer sides. The emission level also appears to be lower between $\psi = 0.6$ and 1.0, thus when the line of sight points both towards the primary inner side or the secondary outer side. The second possibility (i.e. an X-ray emission associated with the secondary inner side) therefore seems to best describe the main features of the X-ray light curve, at least qualitatively. In Sect. 6.3, we present a phenomenological model that associates an extra X-ray emission with the secondary inner side.

Using the relations of Berghöfer et al. (1997) and bolometric luminosities from Table 6, we obtained X-ray luminosities of $\log(L_X) = 31.51$ and 30.69 (erg s^{-1}) respectively for the O9 and B1–1.5 components in the band 0.1–2.0 keV. Accounting for the distance modulus of the cluster $DM = 11.07$, this corresponds to unabsorbed fluxes of $f_X = 9.99$ and 1.54×10^{-14} erg cm^{-2} s^{-1}. Though the energy bands considered are slightly different, we can compare these predictions with the values obtained from the X-ray spectral fits (Table 8). It appears that, even at its minimum of emission ($\psi \sim 0.82$), CPD – 41° 7742 is at least twice brighter than expected from the Berghöfer et al. relations. Part of the gap between the observed and predicted values could however be filled by the following considerations. First, the dispersion around the Berghöfer et al. relations is quite large and does not allow an accurate determination of the X-ray luminosities. Second, Massa et al. (1984) reported that the winds from the main sequence B stars in NGC 6231 are particularly strong. The B star in CPD – 41° 7742 could thus have a particularly powerful wind for its spectral type, producing stronger shocks within its lower layers and, subsequently, an enhanced X-ray emission. Sana et al. (2005b) further reported that, in NGC 6231, the B stars seem to follow a brighter L_X/L_{bol} relation than predicted from Berghöfer et al. (1997). From this new relation, the B1-1.5 component in CPD – 41° 7742 could be at least three times brighter, yielding a luminosity of a few 10^{31} erg s^{-1}.

Table 7. Results of the simultaneous fits of the MOS1 and MOS2 spectra with XSPEC. The model used is wabs$_{\rm ISM}$ * (wabs$_1$ * mekal$_1$ + wabs$_2$ * mekal$_2$). The term wabs$_{\rm ISM}$ was fixed to the interstellar value ($N_{\rm H,ISM} = 0.28 \times 10^{22}$ cm^{-2}); wabs$_1$ was hold to zero ($N_{\rm H,1} = 0$ cm^{-2}, see text). The first and second columns give the phase and the observation number. The next six columns (Cols. 3 to 8) provide the best-fit parameters while Col. 9 lists the corresponding reduced chi-square and the associated number of degrees of freedom (d.o.f.). $N_{\rm H}$ yields the absorbing column (in units 10^{-22} cm^{-2}), kT is the model temperature (in keV) while *norm* is the normalisation factor (expressed in 10^{-4} cm^{-5}, $norm = \frac{10^{-14}}{4\pi d^2} \int n_e n_{\rm H} dV$ with d, the distance to the source – in cm, n_e and $n_{\rm H}$, the electron and hydrogen number densities – in cm^{-3}). Columns 10 to 13 provide the observed fluxes (in 10^{-14} erg cm^{-2} s^{-1}) in the 0.5–10.0 keV energy band and in the $S_{\rm X}$, $M_{\rm X}$ and $H_{\rm X}$ bands respectively. The last line of this table provides the best-fit parameters adjusted on the spectra extracted from the cumulated six pointings.

ψ	Obs. #	$N_{\rm H,1}$	kT_1	$norm_1$	$N_{\rm H,2}$	kT_2	$norm_2$	χ^2_ν (d.o.f.)	$f_{\rm X}$	$f_{\rm X,S}$	$f_{\rm X,M}$	$f_{\rm X,H}$
[1]	[2]	[3]	[4]	[5]	[6]	[7]	[8]	[9]	[10]	[11]	[12]	[13]
0.113	2	0.0	$0.62^{+.06}_{-.08}$	$0.81^{+.15}_{-.13}$	$0.79^{+.33}_{-.28}$	$1.22^{+.26}_{-.17}$	$2.71^{+.74}_{-.70}$	0.63 (59)	21.0	5.6	11.5	3.8
0.278	5	0.0	$0.52^{+.14}_{-.18}$	$0.65^{+.09}_{-.10}$	$0.74^{+.25}_{-.19}$	$0.97^{+.27}_{-.13}$	$1.64^{+.42}_{-.52}$	1.21 (60)	13.0	4.7	7.0	1.3
0.468	3	0.0	$0.52^{+.10}_{-.17}$	$0.66^{+.09}_{-.10}$	$0.76^{+.18}_{-.16}$	$0.95^{+.12}_{-.13}$	$2.28^{+.65}_{-.56}$	0.82 (81)	15.4	4.9	8.7	1.8
0.668	6	0.0	$0.61^{+.05}_{-.14}$	$0.75^{+.14}_{-.28}$	$0.74^{+.41}_{-.36}$	$0.93^{+.36}_{-.35}$	$1.17^{+2.10}_{-.52}$	0.85 (64)	12.7	5.3	6.5	0.9
0.819	1	0.0	$0.40^{+.10}_{-.08}$	$0.76^{+.14}_{-.20}$	$0.52^{+.27}_{-.21}$	$0.81^{+.12}_{-.21}$	$0.94^{+.48}_{-.21}$	1.08 (53)	10.2	5.0	4.7	0.5
0.930	4	0.0	$0.35^{+.19}_{-.09}$	$0.63^{+.30}_{-.23}$	$0.46^{+.19}_{-.16}$	$0.75^{+.14}_{-.08}$	$1.61^{+.49}_{-.48}$	1.22 (46)	11.8	5.2	6.0	0.6
Merged		0.0	$0.59^{+.03}_{-.09}$	$0.74^{+.06}_{-.08}$	$0.73^{+.13}_{-.11}$	$1.05^{+.11}_{-.08}$	$1.39^{+.20}_{-.10}$	1.09 (209)	14.0	5.2	7.3	1.5

Table 8. Unabsorbed fluxes (in 10^{-14} erg cm^{-2} s^{-1}), i.e. fluxes corrected for the interstellar absorption ($N_{\rm H,ISM} = 0.28 \times 10^{22}$ cm^{-2}), according to the best-fit models presented in Table 7. The last column gives the total X-ray luminosity (in erg s^{-1}) assuming a distance modulus $DM = 11.07$.

ψ	Obs. #	$f_{\rm X}^{\rm unabs}$	$f_{\rm X,S}^{\rm unabs}$	$f_{\rm X,M}^{\rm unabs}$	$f_{\rm X,H}^{\rm unabs}$	$\log (L_{\rm X})$
[1]	[2]	[3]	[4]	[5]	[6]	[7]
0.113	2	36.2	16.4	15.8	4.0	32.06
0.278	5	25.4	14.2	9.8	1.4	31.91
0.468	3	28.7	14.8	12.1	1.8	31.96
0.668	6	25.8	15.5	9.3	1.0	31.92
0.819	1	23.8	16.4	6.9	0.5	31.88
0.930	4	25.7	16.4	8.7	0.6	31.92
Merged		27.2	15.4	10.3	1.5	31.95

6.2. CPD − 41° 7742 wind properties

The wind properties of the two components of CPD − 41° 7742 are not known. We however used the newly derived physical parameters of the stars to get an insight into their wind strengths. We estimated their mass-loss rates using the mass-loss recipes from Vink et al. (2000, 2001). We obtained, for the primary, $\log (\dot{M}_1) = −7.06$ ($M_\odot$ yr^{-1}). The temperature of the secondary component however falls within the bi-stability jump region. Using the recommendations from Vink et al., we estimated the position of the bi-stability jump to be located at about 22 800 K for the particular stellar parameters of the secondary. This puts the companion on the hot side of the jump, yielding thus $\log (\dot{M}_2) = −8.74$ ($M_\odot$ yr^{-1}). We estimated the terminal wind velocities by first computing the escape velocities and then adopting the average ratio $v_\infty/v_{\rm esc} = 2.6$ as appropriate for the winds of the stars on the hot side of the stability jump. We respectively obtained terminal velocities of $v_{\infty,1} = 2380$ km s^{-1} and $v_{\infty,2} = 2150$ km s^{-1} for the two components of CPD − 41° 7742. While these values are typical for O-type stars, the secondary terminal velocity seems quite large for a typical B1 dwarf. As stated above, Massa et al. (1984) reported particularly strong winds for the B dwarfs in NGC 6231. For example, they derived, for the single B1 V star CPD−41° 7719, a terminal wind velocity close to 2300 km s^{-1}, thus very near our estimate for the B component in CPD − 41° 7742.

6.3. A wind interaction in CPD − 41° 7742

Using the estimated wind parameters, we computed the position of the ram pressure equilibrium surface that typically indicates the location of a possible wind-wind collision. For this purpose, we adopted a $\beta = 1$ velocity law, as appropriate for the hot star winds. Due to its larger mass-loss rate, the primary wind clearly overwhelms the secondary wind and no equilibrium is possible. In consequence, the O-star wind should crash into the B-star surface, preventing the secondary wind to develop towards the primary star. Under the above hypotheses, the primary wind luminosity at the distance of the secondary surface is about $\log (L_{\rm w,1}) = \log (\frac{\dot{M}_1 v_1^2}{2}) \sim 34.7$ (erg s^{-1}). Accounting for the secondary radius and its distance to the primary, a fraction of about 2.7% of the O9 V wind is intercepted by the secondary and we therefore expect the shocked plasma to be heated to temperatures of a few 10^7 K, thus generating a substantial amount of X-rays. According to the formalism of Usov (1992), and using a primary wind pre-shock velocity of 1380 km s^{-1}, the X-ray emission generated by such a wind-photosphere interaction should be about $\log (L_{\rm X}) \approx 32.8$ (erg s^{-1}) for a purely radiative interaction (Usov's Eq. (80)) and $\log (L_{\rm X}) \approx 30.7$ (erg s^{-1}) in the adiabatic case (Usov's Eq. (79), adopting a solar chemical composition for the wind). Following Stevens et al. (1992),
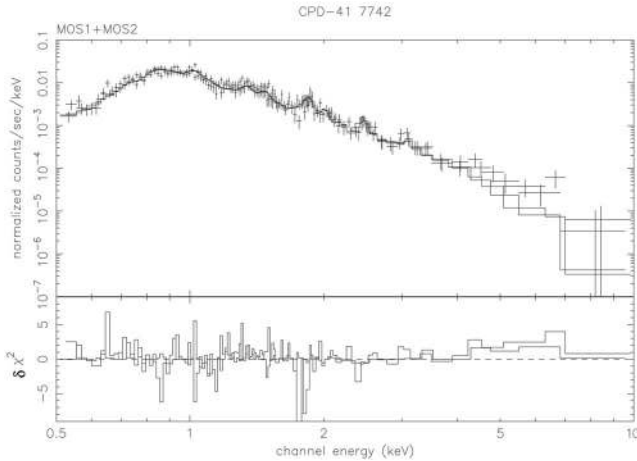
Fig. 10. Least square simultaneous fits of the cumulated MOS1 and MOS2 spectra of CPD – 41° 7742 with absorbed 2-T `mekal` models. The bottom panel shows the contributions of individual bins to the χ^2 of the fit. The contributions are carried over with the sign of the deviation (in the sense data minus model).

the ratio between the characteristic cooling time and flow time is $\chi = t_{\text{cool}}/t_{\text{flow}} \approx 5.2$, indicating a mainly adiabatic collision.

However, the interaction region is immersed in the intense UV photon field of the secondary. Inverse Compton cooling (Comptonization) could thus be significant, yielding a higher cooling rate, thus a lower value for the χ parameter. In addition, under the influence of the radiative pressure of the secondary, the acceleration of the primary wind may be slowed down (the so-called *radiative inhibition* effect, Stevens & Pollock 1994). According to the formalism developed by these latter authors, the mass-loss rate on the axis should not be affected by more than 1%. From a crude interpolation of their results, the primary wind velocity at the secondary surface might however be reduced by about one third. In consequence, the wind kinetical energy would be cut down by a factor of about two. Hence, radiative inhibition might significantly affect the value of the χ parameter, which depends on the fourth power of the velocity. Assuming a factor 2/3 on the velocity reached by the primary wind at the distance of the secondary surface, we obtain $\chi \approx 1.0$. Both under the influence of Comptonization and of radiative inhibition, the shock region might thus shift towards the radiative regime.

Using the formalism of Gayley et al. (1997), we also investigated the possibility to alter the wind-photosphere interaction by sudden radiative braking. In such a phenomenon, the wind of the primary star could be suddenly brought to a stop due to the radiative pressure coming from the companion. The main effect of radiative braking is to modify the position of the dynamical ram pressure equilibrium surface by pushing it further away from the secondary star. In certain cases, radiative braking could be strong enough to prevent the primary star wind to actually reach the secondary surface, thus yielding a wind-wind interaction structure rather than a wind-photosphere interaction. Adopting the known stellar parameters, we computed the radiative braking coefficient. We then used different values of the CAK parameters (Castor et al. 1975) appropriate for effective temperatures around 30 kK. According to the values of

these coefficients as given by different authors (Pauldrach et al. 1986; Shimada et al. 1994; Puls et al. 2000), the radiative braking can, or can not, disrupt the wind-photosphere interaction. It is thus impossible to conclude on this point. However, even when the braking occurs, the interaction is moved only slightly away from the secondary star surface. Though the shock structure would be quite different, the geometry of the emitting region will probably remain rather similar, with an extra emission component mainly located close to the secondary inner surface.

A phenomenological model

To estimate the influence of such a wind interaction on the observed X-ray light curve, we built a simple geometrical model presented in Fig. 11. We adopted a circular orbit, spherically symmetric stars and winds, and a $\beta = 1$ acceleration law for the primary wind. Assuming a totally radiative interaction, we considered that, when encountering the secondary star surface, the kinetic energy associated to the normal velocity component of the incident wind flow is totally dissipated into thermal energy. We thus computed the amount of energy re-emitted by each elements of the secondary surface. Then, accounting for the orbital inclination and the possible occultation by the primary star, we computed the interaction contribution to the observed X-ray light curve. We noticed above the possibility of radiative braking to occur within the system. We caution however that it should not alter much this simple model. Indeed, in the case of a wind-wind collision, the interaction region should still be located near the secondary star surface, so that the geometry of the problem would be only slightly modified. The emission from the secondary shock would further be very limited. Indeed, so close to the surface, the radiative acceleration could not have been very efficient yet. The secondary wind velocity is thus probably of the order of the photospheric thermal velocity, therefore close to $20\,\text{km s}^{-1}$. Under these hypotheses, the possible contribution of the secondary shock to the total X-ray emission would thus be about $10^{29}\,\text{erg s}^{-1}$, at least one order of magnitude below the other emission components.

The results of this simple model are presented in Fig. 12 (upper panel) and provide an upper limit on the actual contribution of such an interaction. Indeed, as stated above, the interaction is probably not fully radiative, so that only a fraction of the incoming energy is effectively radiated. Radiative inhibition might also reduce the wind velocity, giving rise to a weaker shock, hence to a weaker emission than considered here. In Fig. 12, the occultation of the interaction zone by the primary is clearly seen ($\psi \sim 0.35$), while the interaction does not provide any contribution when the secondary is turning its outer side to the observer ($\psi \sim 0.8 - 0.9$). In this simple form, this phenomenological model indeed predicts the higher emission slightly before and after the secondary eclipse, while the secondary inner side is facing the observer, and the lower emission state half a cycle later, when the interaction zone is hidden by the secondary body. It also reasonably reproduces the width of the observed *eclipse* in the X-ray light curve.

In a second step, we try to provide a moderate tuning to the model, in order to investigate to which degree it can match
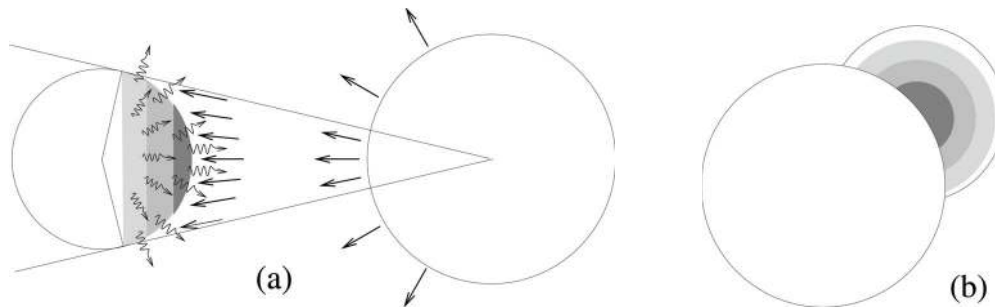
Fig. 11. Schematic view of the geometrical wind-photosphere interaction model in CPD $-41°$ 7742. **a)** A view from above the orbital plane: the secondary star intercepts a small fraction of the primary wind, of which part of the kinetic energy is turned into heat. **b)** A similar view along the line of sight. The different degrees of shading of the secondary surface represent the different X-ray luminosities, these latter being larger closer to the system axis.

the observed modulations. According to the model, no emission from the interaction is expected around $\psi = 0.8-0.9$, and it should only provide a faint contribution at the time of the secondary minimum. At those particular phases, we thus probably observe the intrinsic emission of the two stars which, as explained above, is only slightly affected by the eclipses because of its wide extension. Correcting the observed light curve for the limited encircled energy fraction, the intrinsic emission from the two stars gives about 14×10^{-3} cnt s^{-1} in the two MOS instruments. From Table 7, this approximately corresponds to an observed flux about 10.2×10^{-14} erg cm^{-2} s^{-1}. We also note that the model provides unabsorbed fluxes while the observed count rates have suffered interstellar absorption. Comparing the values of the absorbed and unabsorbed fluxes (Tables 7 and 8), we estimate the ISM material to absorb about half of the flux at the considered energy.

At this stage, the model predicts an emission rate still much larger than the observed emission. To properly match the observations, we have to divide the predicted flux again by a factor of 6, so that the maximum contribution of the interaction zone to the observed flux is now about 10×10^{-14} erg cm^{-2} s^{-1}. This last step finds a relative justification in the fact that, as discussed above, the present purely radiative model only provides an upper limit to the X-ray emission emerging from the interaction zone. In addition, effects that might reduce the shock strength, such as radiative inhibition, are not accounted for. Assuming radiative braking to take place, one might also think that some emission may originate from the trailing arm of the shock cone. In such a configuration, the extra emission from the collision would not drop to zero around $\psi \sim 0.8-0.9$. In the current fully radiative model, the plasma immediately cools down after the shock. By nature, it could thus not produce an extra-emission at these particular phases. Such a contribution from the arms of the shock cone would however be less affected by the eclipses in the system and, as a first approximation, one can consider that it has been accounted for in the empirical pedestal adopted in Fig. 12. This latter is indeed higher than expected from the sole Berghöfer et al. (1997) relations for the intrinsic emission of the early-type stars in the system.

It is clear that the reality is probably different from this idealized situation. It is not our purpose to over-interpret the present model; our aim was to show that, using reasonable

assumptions, an interaction region located on, or near, the secondary surface can reproduce the main features of the observed X-ray light curve.

From Fig. 12, the time of the beginning of the X-ray eclipse is well reproduced by our model. The right wing of the eclipse is however slightly larger, suggesting that the interaction is more extended on the surface side opposite to the orbital motion. Similarly, the drop in emission around $\psi \approx 0.6$ occurs slightly later than expected from our model, which means that the X-ray emitting region should remain visible slightly longer, a condition which does not tally with the previous suggestion. Clearly, Fig. 12 shows that the observed modulations in the X-ray light curves is dominated by an extra-emission component associated with the secondary inner surface. However, the details of the phenomenon could be more complicated as suggested by the observed delays in the rising and falling branches near $\psi = 0.4$ and 0.6. Finally, the hardness ratio curves indicate that the hardest emission is observed at the time of the two emission maxima. This is expected if the extra emission is produced in a wind interaction region, which provides typically harder X-rays than the intrinsic emission from the stars.

7. Final remarks and conclusions

In the first part of this paper, we presented optical photometry of CPD $-41°$ 7742. Adopting the period obtained from Paper I, the analysis of the system light curves indicates that CPD $-41°$ 7742 is a well detached system with an inclination close to $77°$. The obtained curves display two eclipses with a separation slightly different from half an orbital cycle, thus indicating a small eccentricity, in agreement with the results of Paper I. Combining the spectroscopic and photometric analyses, we derived the absolute physical parameters of the stellar components and confirmed that the system is formed by two dwarf early-type stars with masses, sizes and luminosities relatively close to typical values expected both from observational and theoretical works.

The photometric and spectroscopic data sets however provide discrepant values for the longitude of periastron. Independent observations by Sterken & Bouzid (2004) also tend to indicate either a periastron argument close to 90 or $270°$ or a zero eccentricity. Their light curves, obtained over at least two years, also display intriguing signs of variability. Clearly,
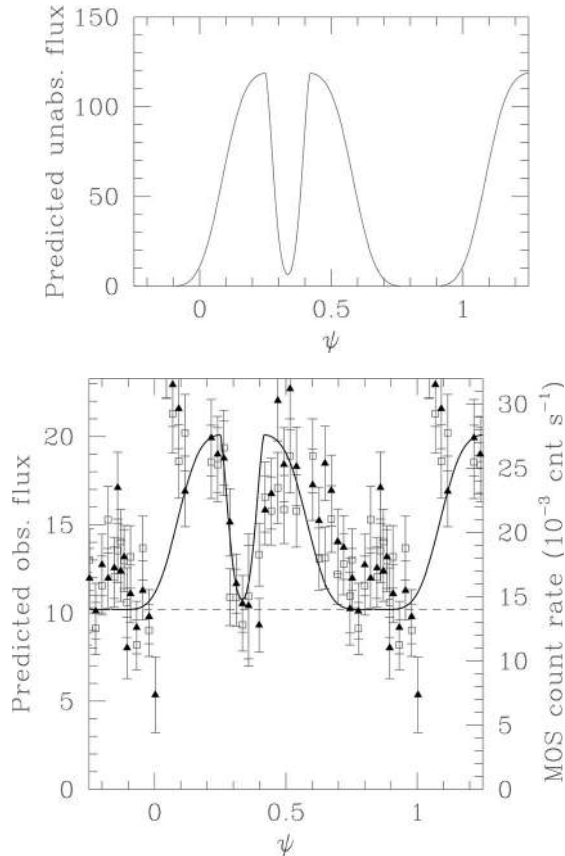
Fig. 12. *Upper panel*: predicted unabsorbed flux emitted by a radiative wind-photosphere interaction in CPD − 41° 7742. *Lower panel*: tuned phenomenological model (thick line) overplotted on the observed X-ray light curves. Filled triangles and open squares respectively show the background-corrected EPIC MOS1 and MOS2 count rates in the 0.5–10.0 keV energy band. These count rates have been corrected for the limited size of the extraction region. Flux axes are in units of 10^{-14} erg cm^{-2} s^{-1} in both panels. The dashed line gives the adopted intrinsic contribution from the two stellar components of CPD − 41° 7742. It acts as a pedestal.

further observations are needed to elucidate these apparent discrepancies.

In the second part of the present paper, we focused on recent XMM-*Newton* X-ray observations of the system. The X-ray emission from CPD − 41° 7742 is well described by a two-temperature thermal plasma model with energies close to 0.6 and 1.0 keV, thus slightly harder than typical emission from early-type stars. The X-ray light curve of the system is clearly variable both in the total and in the different energy ranges; the emission level is higher when the primary is in front of the secondary. During the high state, the system shows a drop of its X-ray emission that almost exactly matches the optical secondary eclipse. Assuming that the X-ray light curve is reproducible, we interpreted this as the signature of a wind interaction phenomenon in which the overwhelming primary wind crashes into the secondary star surface. Alternatively, the wind-photosphere interaction could be altered by sudden radiative braking, yielding a wind-wind interaction located close to the secondary surface, and displaying thus a similar geometry. We expect this phenomenon to produce a substantial amount

of X-rays, which could be the major source for the observed modulations in the EPIC MOS light curves. As a next step, we built a simple phenomenological model that associates an extra X-ray emission component with the inner side of the secondary star surface. Though limited by some simplifying assumptions, this model renders the main properties of the observed variations and lends thus further support to our interpretation of the X-ray light curve.

At this stage, several important questions remain however unanswered. The exact influence of the wind interaction, and of the generated X-ray emission, on the secondary surface properties is very difficult to estimate. We carefully inspected the high resolution high signal to noise spectra from Paper I but could not find any systematic differences in the secondary spectra obtained when this star is showing either its inner or its outer face to the observer. As a final check, we put a point-like X-ray source at a distance of $1.1 \times R_2$ from the center of the secondary star on the system axis. We assigned to this source a luminosity of 10^{33} erg s^{-1}, which is probably typical of the wind interaction taking place in the system. The additional heating of the secondary star surface elements closest to the X-ray source amounts to a few tens of Kelvin. For comparison, the heating of the same surface elements by the radiation of the primary component, is about 2000–2500 K. This clearly suggests that the heating of the secondary surface by the nearby interaction should be limited.

Formed by an O9 plus a B1–1.5 dwarf, CPD − 41° 7742 a priori seemed to be an ordinary, well detached system. We however showed that it probably harbours a wind-wind or wind-photosphere interaction. Such a phenomenon could be quite common among close early-type systems. It is thus of a particular importance to evaluate its possible impact on the determination of the physical parameters obtained using different observational methods. The possible variable activity of CPD − 41° 7742 is an additional motivation to accumulate more data on this particularly interesting early-type binary system.

Finally, the present set of observations provides X-ray light curves that cover almost the full orbital cycle of CPD − 41° 7742 with reasonable signal-to-noise and time resolution. As discussed in Sect. 6.3, different physical phenomena (radiative inhibition, radiative braking, Comptonization, ...) probably affect the shock structure and, hence, the exact amount of X-ray emission generated by the wind interaction. The development of appropriate tools, both theoretical and numerical, to analyse such *high quality* X-ray light curves is probably one of the challenges that the new generation of X-ray stellar scientists will have to face in the coming decade, especially to prepare the ground for the next generation of large X-ray observatories.

References

Antokhina, E. A. 1988, AZh, 65, 1164

Antokhina, E. A. 1996, Astron. Rep., 40, 483

Arnaud, K. A. 1996, in Astronomical Data Analysis Software and Systems V, ed. G. Jacoby, & J. Barnes, ASP Conf. Ser., 101, 17

Balona, L. A., & Laney, C. D. 1995, MNRAS, 276, 627

Barr, J. 1908, JRASC, 2, 70

Batten, A. H. 1983, JRASC, 77, 95

Batten, A. H. 1988, PASP, 100, 160

Baume, G., Vázquez, R. A., & Feinstein, A. 1999, A&AS, 137, 233

Bell, S. A., Hilditch, R. W., & Adamson, A. J. 1987, MNRAS, 225, 961

Berghöfer, T. W., & Schmitt, J. H. M. M. 1994, Ap&SS, 221, 309

Berghöfer, T. W., Schmitt, J. H. M. M., Danner, R., & Cassinelli, J. P. 1997, A&A, 322, 167

Bianchi, L., & Garcia, M. 2002, ApJ, 581, 610

Burkholder, V., Massey, P., & Morrell, N. 1997, ApJ, 490, 328

Castor, J. I., Abbott, D. C., & Klein, R. I. 1975, ApJ, 195, 157

Crowther, P. A., Hillier, D. J., Evans, C. J., et al. 2002, ApJ, 579, 774

Diaz-Cordoves, J., & Gimenez, A. 1992, A&A, 259, 227

Diaz-Cordoves, J., Claret, A., & Gimenez, A. 1995, A&AS, 110, 329

Feldmeier, A., Puls, J., & Pauldrach, A. W. A. 1997, A&A, 322, 878

Fracastoro, M. G. 1979, A&A, 78, 112

Gayley, K. G., Owocki, S. P., & Cranmer, S. R. 1997, ApJ, 475, 786

Gies, D. R. 2003, in A Massive Star Odyssey: from main sequence to supernova, ed. K. van der Hucht, A. Herrero, & C. Esteban, IAU Symp., 212, 91

Herrero, A. 2003, in A Massive Star Odyssey: from main sequence to supernova, ed. K. van der Hucht, A. Herrero, & C. Esteban, IAU Symp., 212, 3

Herrero, A., Kudritzki, R. P., Vilchez, J. M., et al. 1992, A&A, 261, 209

Herrero, A., Puls, J., & Najarro, F. 2002, A&A, 396, 949

Hill, G., & Holmgren, D. E. 1995, A&A, 297, 127

Himmelblau, D. M. 1971, Applied Nonlinear Programming (New-York: McGraw-Hill)

Howarth, I. D. 1993, The Observatory, 113, 75

Howarth, I. D., & Prinja, R. K. 1989, ApJS, 69, 527

Humphreys, R. M., & McElroy, D. B. 1984, ApJ, 284, 565

Jansen, F., Lumb, D., Altieri, B., et al. 2001, A&A, 365, L1

Kaastra, J. 1992, An X-Ray Spectral Code for Optically Thin Plasmas, Internal SRON-Leiden Report, updated version 2.0

Kallrath, J., & Linnell, A. P. 1987, ApJ, 313, 346

Manfroid, J. 1993, A&A, 271, 714

Manfroid, J. 1995, A&AS, 113, 587

Manfroid, J., Royer, P., Rauw, G., & Gosset, E. 2001, in Astronomical Data Analysis Software and Systems X, ed. F. Harnden, F. Primini, & H. Payne, ASP Conf. Ser., 238, 373

Martins, F., Schaerer, D., & Hillier, D. J. 2002, A&A, 382, 999

Massa, D., Savage, B. D., & Cassinelli, J. P. 1984, ApJ, 287, 814

Mewe, R., Gronenschild, E. H. B. M., & van den Oord, G. H. J. 1985, A&AS, 62, 197

Pauldrach, A., Puls, J., & Kudritzki, R. P. 1986, A&A, 164, 86

Popper, D. M., & Hill, G. 1991, AJ, 101, 600

Puls, J., Springmann, U., & Lennon, M. 2000, A&AS, 141, 23

Rauw, G., Sana, H., Antokhin, I. I., et al. 2001, MNRAS, 326, 1149

Royer, P., Vreux, J.-M., & Manfroid, J. 1998, A&AS, 130, 407

Sana, H., Hensberge, H., Rauw, G., & Gosset, E. 2003, A&A, 405, 1063

Sana, H., Stevens, I. R., Gosset, E., Rauw, G., & Vreux, J.-M. 2004, MNRAS, 350, 809

Sana, H., Gosset, E., Rauw, G., Sung, H., & Vreux, J.-M. 2005a, A&A, in press

Sana, H., Nazé, Y., Gosset, E., et al. 2005b, in Massive Stars in Interacting Binaries, ed. A. Moffat, & N. St-Louis, ASP Conf. Ser., 5, in press

Schaller, G., Schaerer, D., Meynet, G., & Maeder, A. 1992, A&AS, 96, 269

Schmidt-Kaler, T. 1982, Landolt-Börnstein, Numerical Data and Functional Relationships in Science and Technology, New Series, Group VI, Vol. 2b, Physical Parameters of the Stars (Berlin: Springer-Verlag)

Shimada, M. R., Ito, M., Hirata, B., & Horaguchi, T. 1994, in Pulsation; Rotation; and Mass Loss in Early-Type Stars, ed. L. Balona, H. Henrichs, & J. Contel, IAU Symp., 162, 487

Simon, K. P., Sturm, E., & Fiedler, A. 1994, A&A, 292, 507

Sterken, C., & Bouzid, M. Y. 2004, in Rev. Mex. Astron. Astrofis., Compact Binaries in the Galaxy and Beyond, ed. G. Tovmassian, & E. Sion, Conf. Ser., 20, 79

Stetson, P. B. 1987, PASP, 99, 191

Stevens, I. R., & Pollock, A. M. T. 1994, MNRAS, 269, 226

Stevens, I. R., Blondin, J. M., & Pollock, A. M. T. 1992, ApJ, 386, 265

Struve, O. 1948, PASP, 60, 160

Sung, H., Bessell, M. S., & Lee, S. 1998, AJ, 115, 734

Turner, M. J. L., Abbey, A., Arnaud, M., et al. 2001, A&A, 365, L27

Usov, V. V. 1992, ApJ, 389, 635

Vacca, W. D., Garmany, C. D., & Shull, J. M. 1996, ApJ, 460, 914

van Hamme, W. 1993, AJ, 106, 2096

Vaz, L. P. R., Cunha, N. C. S., Vieira, E. F., & Myrrha, M. L. M. 1997, A&A, 327, 1094

Vink, J. S., de Koter, A., & Lamers, H. J. G. L. M. 2000, A&A, 362, 295

Vink, J. S., de Koter, A., & Lamers, H. J. G. L. M. 2001, A&A, 369, 574

Wilson, R. E. 1979, ApJ, 234, 1054

Zinnecker, H. 2003, in A Massive Star Odyssey: from main sequence to supernova, ed. K. van der Hucht, A. Herrero, & C. Esteban, IAU Symp., 212, 80